

Anomalous ellipticity dependence of the generation of near-threshold harmonics in noble gases

Bincheng Wang,¹ Yinfu Zhang,¹ Pengfei Lan,^{1,*} Chunyang Zhai^{①,2}, Min Li,¹ Xiaosong Zhu,¹ Jing Chen,^{3,4,†}
Peixiang Lu^{①,1,5,‡} and C. D. Lin^{①,6}

¹*School of Physics and Wuhan National Laboratory for Optoelectronics, Huazhong University of Science and Technology, Wuhan 430074, China*

²*College of Physics and Electronic Engineering, Xinyang Normal University, Xinyang 464000, China*

³*HEDPS, Center for Applied Physics and Technology, Peking University, Beijing 100084, China*

⁴*Institute of Applied Physics and Computational Mathematics, P. O. Box 8009, Beijing 100088, China*

⁵*Hubei Key Laboratory of Optical Information and Pattern Recognition, Wuhan Institute of Technology, Wuhan 430205, China*

⁶*Department of Physics, Kansas State University, Manhattan, Kansas 66506, USA*



(Received 26 December 2020; accepted 10 May 2021; published 24 May 2021)

We measured the ellipticity dependence of the harmonic yield of He, Ne, Ar, Kr, and Xe. It is found that the harmonic yield in general decreases monotonically with increasing laser ellipticity but anomalous dependence does occur for each atom for some harmonic orders. We found that the degree of anomaly is weakest in helium but is stronger for the heavier atoms. The anomaly also depends on laser intensity. To explain these features, we developed a quantum trajectory Monte Carlo (QTMC) model based on the quantum path integral theory to study high-order harmonic generation (HHG). The model includes the effect of Coulomb potential from the target ion, thus it is capable of calculating near-threshold harmonics quantitatively. This model reveals that the presence of Coulomb potential would generate orbiting trajectories which are responsible for the anomalous ellipticity dependence near the threshold.

DOI: [10.1103/PhysRevA.103.053119](https://doi.org/10.1103/PhysRevA.103.053119)

I. INTRODUCTION

High-order harmonic generation (HHG) is a fundamental atomic and molecular process in strong laser fields that plays a crucial role in the development of ultrafast science and technology [1–3]. HHG not only serves as a coherent light source in the extreme ultraviolet (XUV) range [4–7] but also provides a useful tool for probing ultrafast electronic structure and dynamics of atoms or molecules [8–13]. For harmonics that are above the ionization energy I_p , they can be understood by the three-step model [14,15]: first, the electron is freed by a strong laser field. Then it is accelerated in the laser field. Finally, when the electron returns to the parent ion, it may recombine with the ion core and the energy it obtained in the laser field is emitted in the form of high-order harmonics. The three-step model provides an intuitive understanding of the harmonics in the plateau and cutoff region qualitatively. It can also be understood well by the strong-field approximation (SFA) of Lewenstein *et al.* [16].

More recently, attention has been directed at near-threshold harmonics (NTHs). These harmonics offer great potential as possible light sources for vacuum-ultraviolet frequency combs [17–20]. However, the mechanism of NTH is still not well understood. Chini *et al.* [17] measured the NTH spectrum of Ar and proposed that resonantly enhanced excitation makes

a great contribution to the NTH of Ar. On the other hand, Xiong *et al.* [21–23] suggested that, in addition to resonantly enhanced excitation, the NTH is also affected by the rescattering process. The NTH is understood by a four-step model: (1) ionization, (2) acceleration in the laser field, (3) trapping in the excited states after returning to the core, and (4) subsequent emission of a photon. The excited states are usually considered to be Rydberg states [24]. A similar process also happens in strong-field ionization, which is called frustrated ionization [20,25,26]. Moreover, Yost *et al.* found that the 7th, 9th, 11th, and 13th harmonic yields of Xe generated from a 1070 nm laser field are roughly proportional to the sixth power of the driving laser intensity. To explain the laser intensity dependence, they proposed a quantum path interference method for the NTH generation [5,27].

To test whether the three-step model can effectively explain the generation of NTH, experiments have been carried out using elliptically polarized laser fields [28–34]. Anomalous ellipticity dependence of harmonic yield for NTH has been reported for different atoms and molecules. Different from the harmonics in the plateau region, the NTH yield does not drop monotonically with increasing laser ellipticity. Avnani *et al.* [34] measured the ellipticity dependence of the NTH yield of He, Ne, Ar, and Kr and explained that the anomalous ellipticity dependence is due to the multiwave mixing process. Anomalous ellipticity dependence is also observed in molecules. Soifer *et al.* [31] measured the ellipticity dependence of the NTH yield of O₂ and suggested that the anomalous ellipticity dependence originates from resonantly enhanced excitation. Furthermore, it has been proposed that

*pengfeilan@hust.edu.cn

†chen_jing@iapcm.ac.cn

‡lupeixiang@hust.edu.cn

the Coulomb potential will affect the interference between the two quantum paths, which would lead to an enhancement of NTH in Ne [33].

From the theory side, the analysis of NTH so far has not been fully supported by quantitative calculations, for example, the species dependence. It is generally considered that the time-dependent Schrödinger equation (TDSE) can be used to calculate the NTH, but such calculations are very time consuming and do not offer the possibility of understanding the generation mechanism. The SFA is easier to calculate but is not accurate enough in the near-threshold region because of the neglect of the Coulomb potential. The Coulomb correction model in Ref. [33] cannot explain the atomic species dependence observed in Ref. [28], nor our experiment reported here.

In this paper, we measure the ellipticity dependence of the harmonic yield of He, Ne, Ar, Kr, and Xe. Different from the previous work [34], in our experiment, anomalous ellipticity dependence varies with atomic species and laser intensity. These results cannot be explained by previous mechanisms. We propose a quantum trajectory Monte Carlo (QTMC) model for HHG that can be used to calculate the NTH [35,36]. The Coulomb potential and species-dependent transition dipoles are taken into consideration in our model to study the ellipticity dependence of the NTH. It was found that the results matched well with our experiment. Besides, our method can analyze the electron trajectory individually and calculate the harmonic spectrum generated from specific trajectories, which offers a more intuitive understanding of the mechanism of the NTH generation.

This paper is organized as follows. Section II shows the experimental method. In Sec. III, we introduce our theoretical model. Section IV discusses the results of the experiment and our theoretical interpretations. A summary and outlook are given in Sec. V.

II. EXPERIMENTAL METHOD

We apply a Ti:sapphire laser system (Astrella-USP-1K, Coherent, Inc.) to generate high-order harmonics, which delivers 35-fs, 800-nm pulses at a repetition rate of 1 kHz with the maximum energy of 7 mJ per shot. A half-wave plate and a quarter-wave plate are installed to adjust the polarization state of the laser. The ellipticity ε is controlled by rotating the half-wave plate in front of the fixed quarter-wave plate to keep the major axis of the polarization ellipse fixed. The value of ε is determined by the amplitude ratio of the minor axis and major axis of the elliptically polarized laser field. The total intensity is kept constant throughout the experiment [31]. The laser is focused on a gas jet by a 500 mm focal length lens. The diameter of the nozzle is 100 μm . The laser intensity is estimated from the cutoff law [37,38]. The generated harmonics are dispersed by a 300 grooves/mm grating. The multi-order diffractions of the harmonics with different frequencies have different diffraction angles after the harmonics go through the grating. A possible systematic error of the measured harmonic yield may result from the polarization-dependent reflectivity of the grating. In our experiment, due to the small ellipticity of the generated NTH, the error induced by the grating is about 5%, which is within our measurement error range (7%). Finally, the diffracted harmonics are imaged on the

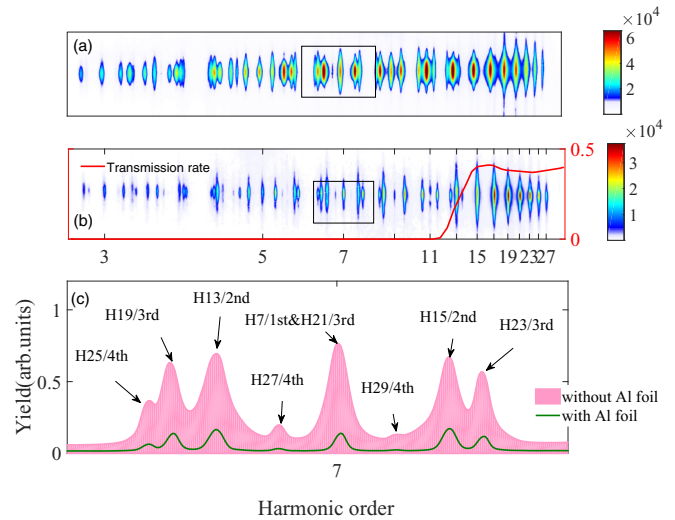


FIG. 1. (a) The harmonic spectrum measured in the experiment without the aluminium foil and (b) with the Al foil. The red line is the transmission coefficient of the Al foil as a function of the harmonic order. (c) The zoom of panels (a) and (b) around the 7th harmonic.

microchannel plate (MCP) fitted with a phosphor screen of 90 mm diameter.

Different from HHG in the plateau and cutoff region, the NTH are harder to observe. Figure 1(a) shows the measured harmonic spectrum. It is found that, except for the first-order diffraction, there also exist some high-order diffractions from the higher-order harmonics. For example, the red line in Fig. 1(c) shows the zoomed-in Fig. 1(a) around the 7th harmonic. It is found that the 7th harmonic includes contributions from its first-order diffraction and the third-order diffraction from the 21st harmonic. It is worth noting that the fifth order diffraction from the 35th harmonic and the higher-order diffraction are ignored, because of the low yield of the cutoff-region harmonics ($>33\text{rd}$). Also around the 7th harmonic, we can observe the fourth-order diffraction from the 27th harmonic, the fourth-order diffraction from the 29th harmonic, and so on. To eliminate these obstructions, we installed an Al foil before the diffraction grating. The density of it is 2.6989 g/cm^3 and the thickness is 0.4 microns [39]. The red line in Fig. 1(b) is the transmission of the Al foil as a function of harmonic order and Fig. 1(b) displays the measured harmonic spectrum after the Al foil is installed. One can see that Al foil filters out harmonics below the 11th order and retains higher-order harmonics and their multi-order diffraction signals. For example, the green line in Fig. 1(c) shows the zoomed-in Fig. 1(b) around the 7th harmonic. The signal of the 7th harmonic is filtered out and it only retains the third-order diffraction from the attenuated 21st harmonic. Thus, we can subtract the diffraction signals and obtain the NTH signals using the following formula :

$$I(\omega_{NTH}) = I_{\text{without Al}}(\omega_{NTH}) - I_{\text{with Al}}(\omega_{NTH})/T(\omega_{\text{high}}), \quad (1)$$

where $I(\omega_{NTH})$ is the intensity of the NTH, $I_{\text{without Al}}(\omega_{NTH})$ is the harmonic intensity of the NTH without the Al foil, $I_{\text{with Al}}(\omega_{NTH})$ is the NTH intensity with Al foil and $T(\omega_{\text{high}})$

is the transmission coefficient of the corresponding high-order harmonic.

III. THEORETICAL METHOD

In this section, we introduce our theoretical model. We extend the quantum trajectory Monte Carlo (QTMC) method [36] of strong-field ionization to HHG. Starting with TDSE for one-electron model atom (atomic units are used in this paper),

$$i \frac{\partial}{\partial t} |\psi(\vec{r}, t)\rangle = \hat{H} |\psi(\vec{r}, t)\rangle, \quad (2)$$

$$\hat{H} = \hat{T} + V_c + V_e,$$

here \hat{T} is the electron kinetic energy operator $\hat{T} = -\hat{\nabla}^2/2$, V_c is a soft-core Coulomb potential and the $V_e = \vec{r} \cdot \vec{E}(t)$ is the interaction with the laser field. $\vec{E}(t)$ is the laser electric field. According to path interference theory [40], the wave function at $\vec{r} + \Delta\vec{r}$ and $t + \Delta t$ is

$$|\psi(\vec{r} + \Delta\vec{r}, t + \Delta t)\rangle = U(\vec{r}, t, \vec{r} + \Delta\vec{r}, t + \Delta t) |\psi(\vec{r}, t)\rangle, \quad (3)$$

where $U(\vec{r}, t, \vec{r} + \Delta\vec{r}, t + \Delta t)$ is the propagator. It is defined by the transition-probability amplitude between the two space-time points (\vec{r}, t) and $(\vec{r} + \Delta\vec{r}, t + \Delta t)$:

$$U(\vec{r}, t, \vec{r} + \Delta\vec{r}, t + \Delta t) = \sum_{N, \Delta\vec{r} \rightarrow 0, \Delta t \rightarrow 0} e^{-iS(\Delta\vec{r}, \Delta t)}. \quad (4)$$

The N in this equation represents all the possible quantum paths and S is the integral of the Lagrangian L :

$$S = \int L dt, \quad (5)$$

$$L = T - V_c - V_e = L_0 + L_e,$$

$$L_0 = T - V_c,$$

$$L_e = -V_e.$$

The harmonics are generated from the time-dependent induced dipole between a final state $|\psi_f(\vec{r}, t)\rangle$ and an initial state $|\psi_i(\vec{r}, t_0)\rangle$.

$$d(t) = \langle \psi_f(\vec{r}, t) | \vec{A}(\vec{r}, t) \cdot \vec{\nabla} | \psi_i(\vec{r}, t_0) \rangle, \quad (6)$$

where t_0 is the ionization time. Based on Eqs. (3) and (4), the time-dependent final state $|\psi_f(\vec{r}, t)\rangle$ can be expressed as

$$|\psi_f(\vec{r}, t)\rangle = \sum_N e^{-i \int_0^t (L_0 + L_e) dt} |\psi_i(\vec{r}, t_0)\rangle, \quad (7)$$

Inserting Eq. (7) into Eq. (6), we obtain the time-dependent induced dipole:

$$d(t) = A_0(\omega) \hat{\epsilon} \sum_N \int U_N(E(t), \theta(t)) \sigma_N(E(t), \theta(t)) dr, \quad (8)$$

where $\sigma_N(E(t), \theta(t))$ represents the transition dipole moment of the electron in a potential V_c and is defined as

$$\sigma_N(E(t), \theta(t)) = \frac{1}{(2\pi)^{3/2}} \frac{f^{(\pm)}(\hat{k}(t) \cdot \hat{r}(t))}{\vec{r}(t)} \times \exp(-i\vec{k}(t) \cdot \vec{r}(t)) \vec{\nabla} \psi_i(\vec{r}, t_0), \quad (9)$$

where $\vec{k}(t)$ is the electron momentum as a function of time, $\vec{r}(t)$ is the electron position, $E(t)$ is the energy of the electron, $\theta(t)$ is the angle of the electron momentum, and $f^{(\pm)}(\hat{k}(t) \cdot \hat{r}(t))$ is called the scattering amplitude and can be calculated as given in Ref. [41].

The propagator induced by the laser field is denoted by $U_N(E(t), \theta(t))$ as

$$U_N(E(t), \theta(t)) = e^{-i \int_0^t L_e dt} e^{-\frac{1}{2} i \int_0^t (-i\hbar\vec{k}) dt}. \quad (10)$$

For clarity, the detailed derivation from Eq. (6) to Eq. (8) is given in the Appendix.

The sum in Eq. (8) should include all the possible paths. Similar to the approximation used in the application of QTMC for strong-field ionization, we only consider paths that satisfy the classical Lagrangian equation of motion to calculate the harmonics. The Lagrangian equation is expressed as

$$\frac{d}{dt} \left(\frac{\partial L}{\partial \vec{k}} \right) - \frac{\partial L}{\partial \vec{r}} = F, \quad (11)$$

$$F = -\vec{E}(t) - \frac{\partial V_c}{\partial \vec{r}}.$$

where \vec{k} is the momentum and \vec{r} is the coordinate.

A Monte Carlo method is used to generate at least 1 million electron trajectories that have different ionization times, momenta, and positions. The initial conditions of the electron (position, momentum, and ionization time) are given by the ionization theory, such as the ADK model [42–44] or the PPT model [45]. In this work, we use the ADK model. We then calculate the phase $S = \int_0^t L_e dt$, the propagator $U_N(E(t), \theta(t))$, and the transition dipole moment of the electron, $\sigma_N(E(t), \theta(t))$, of each trajectory. They are multiplied to obtain the induced dipole of each trajectory $d_N(t)$:

$$d_N(t) = \eta_N(\vec{r}, \vec{p}, t) U_N(E(t), \theta(t)) \sigma_N(E(t), \theta(t)), \quad (12)$$

where $\eta_N(\vec{r}, \vec{p}, t)$ is the ionization distribution of the ADK model. The induced dipoles of each trajectory, $d_N(t)$, are superimposed coherently to obtain the final induced dipole:

$$d(t) = A_0(\omega) \hat{\epsilon} \sum_N \int d_N(t) dr. \quad (13)$$

Equations (12) and (13) are similar to the widely used quantitative rescattering theory (QRS) [46]. $\eta_N(\vec{r}, \vec{p}, t)$ is the ionization probability of each trajectory. $U_N(E(t), \theta(t))$ is the propagator induced by the electric field, and its coherent superposition corresponds to the wave packet in QRS. $\sigma_N(E(t), \theta(t))$ is the transition dipole moment of the electron in a potential V_c for the corresponding electron trajectory. Its modulus squared is the cross section which represents the recombination probability of the electron.

Comparing with the classical trajectory Monte Carlo (CTMC) [31,47] method, our model introduces a phase for each trajectory that leads us to a coherent superposition of transitions from all trajectories to obtain harmonics quantitatively, including both their amplitudes and phases. Our method also considers the recombination cross section and the influence of Coulomb potential on the electron trajectory. Thus in principle it can calculate the NTH more accurately.

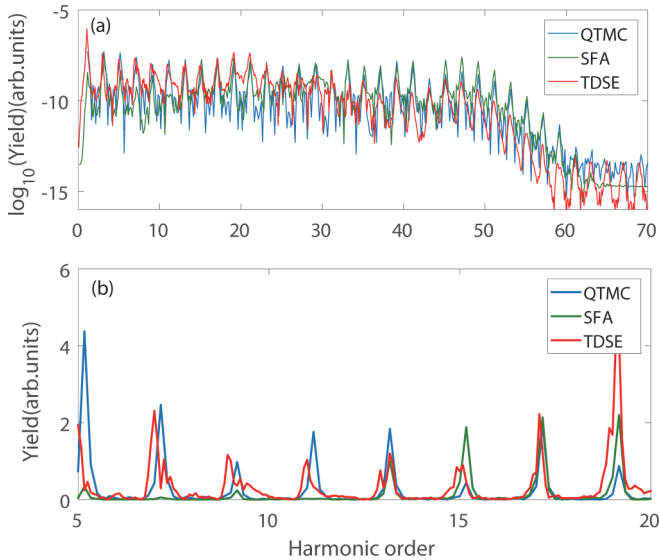


FIG. 2. (a) The harmonic spectrum of atomic hydrogen calculated from the present QTMC method, the TDSE, and the SFA, respectively. (b) The harmonic yield on a linear scale for harmonics near the ionization threshold. The figure shows the failure of the SFA in the near-threshold region and the good agreement between the TDSE and QTMC. The laser is linearly polarized.

We display a comparison of the harmonic spectra calculated by our model, the SFA, and the TDSE in Fig. 2. The harmonic spectra are generated from the interaction between an 800 nm linearly polarized laser field and the hydrogen atom. The laser intensity envelope has a trapezoidal shape with 12 constant cycles, and 2 cycles on and off with peak intensity of 3×10^{14} W/cm². In Fig. 2(a), the harmonics from the three calculations show similar structures, with the plateau and cutoff harmonics at the same positions. The difference lies in the near-threshold region (about the 9th), where harmonics calculated by the SFA model disappear, in disagreement with the TDSE and the present QTMC [see Fig. 2(b)]. In contrast, results from QTMC and TDSE match well. It is worth noting that, with a larger number of electron trajectories, the calculated QTMC results are in better agreement with the TDSE results. We remark that the comparison above between the QTMC and TDSE has been made for linearly polarized lasers. For HHG from elliptically polarized light, the computational demand for solving the TDSE increases significantly because calculations have three spatial dimensions instead of only two spatial dimensions for a linearly polarized laser. For the QTMC calculation, the increase of computing time from linear to elliptical polarization is less severe. Thus, the QTMC method can be used to investigate HHG from elliptically polarized lasers.

IV. RESULTS AND DISCUSSION

Figure 3 shows the measured harmonic yield of Kr as a function of the laser's ellipticity. The harmonic yields for different ellipticity are normalized to the one with ellipticity $\varepsilon = 0$. One can see the ε dependence of the 7th and 9th harmonics (below the threshold) are anomalous. The peak harmonic yield is about 1.11 when ε is about 0.09. For the

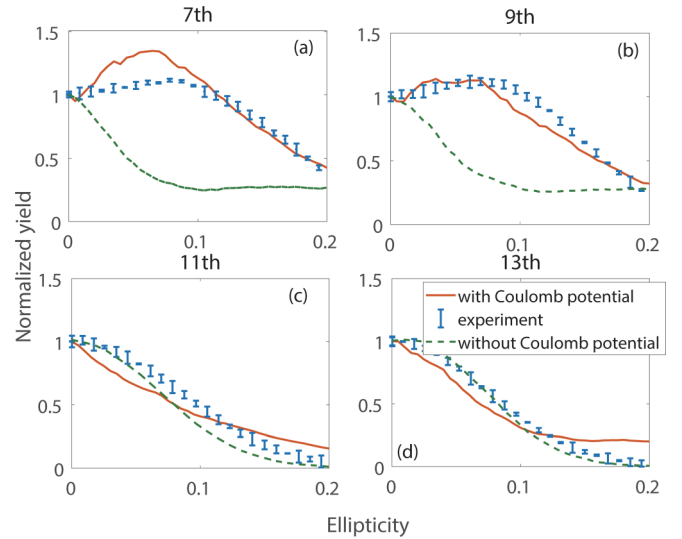


FIG. 3. The measured harmonic yields (normalized, see text) showing anomalous ellipticity dependence. Target is krypton. Experiment: with markers. Theory: QTMC calculations with the Coulomb potential included (red lines) and without (green lines). The importance of the Coulomb potential is clearly seen for harmonic orders seven and nine.

11th and 13th harmonics (above the threshold), the yields decrease monotonically with the increase of ε . The measured results are in good agreement with QTMC calculations.

The red lines in Fig. 3 show the calculated results based on the QTMC method. It is based on a soft-core Coulomb potential where the potential takes a Coulomb form when the electron is a large distance from the core:

$$V_c = \frac{-(1 + 9e^{-r^2})}{\sqrt{r^2 + \alpha^2}}, \quad (14)$$

where α is the soft-core parameter. α is set at 5.60 such that it gives the correct I_p of Kr. In the equation, r represents the distance of the electron from the nucleus. The laser intensity is 2×10^{14} W/cm², which was estimated from the cutoff (33rd) of the harmonic spectrum in the experiment when the laser is linearly polarized. The error of the estimated laser intensity is $\pm 10\%$, which ranged from 1.8 to 2.2×10^{14} W/cm². The error of the estimated laser intensity will lead to a slight variation of the calculated ε dependence but has no influence on our final conclusion. The laser envelope has a trapezoidal shape with 12 constant cycles, and 2 cycles on and off and a wavelength of 800 nm. The harmonic yield increases initially with ε and then decreases for the 7th and 9th harmonics. For the 11th and 13th harmonics, the yields decay monotonically with the increase of ε . Our calculated ellipticity dependence agrees well with the measured one within error. To demonstrate the influence of the Coulomb potential, we calculate the harmonic yield of Kr as a function of ε by removing the asymptotic Coulomb potential. They are shown as green lines in Fig. 3. Clearly, without the Coulomb potential, all harmonics decrease monotonically as ε is increased, thus demonstrating the important role of the Coulomb potential for the anomalous ellipticity dependence for near-threshold harmonics, but less so as the harmonic order is increased.

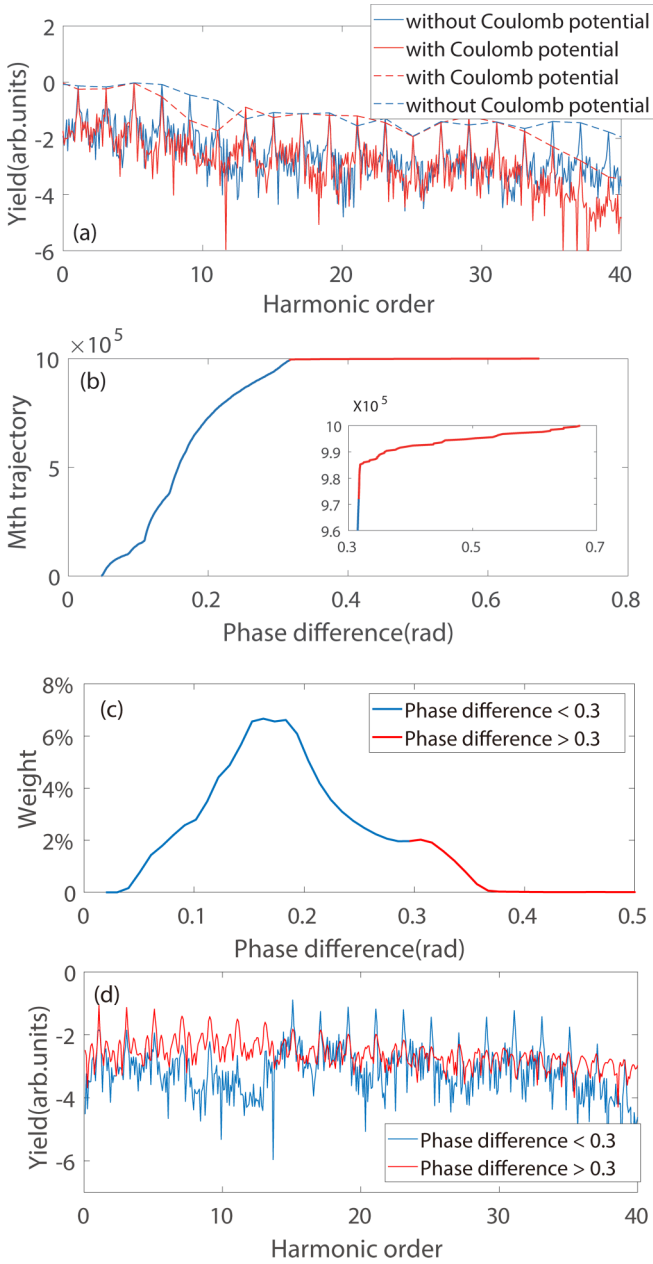


FIG. 4. (a) The calculated harmonic spectra for ellipticity $\varepsilon = 0$. (b) The phase difference of the m th trajectory calculated with and without the Coulomb potential. The inset of panel (b) shows a zoom-in of panel (b) when the phase difference > 0.3 . (c) The weight of the trajectories with different phase difference. (d) The harmonic spectrum generated from trajectories whose phase difference is > 0.3 (red line) versus those where the phase difference is < 0.3 (blue line).

In Fig. 4, we discuss how the Coulomb potential affects the NTH. Figure 4(a) shows the calculated harmonic spectra based on the QTMC model for $\varepsilon = 0$. With the inclusion of the Coulomb potential, the yields of the 7th, 9th, and 11th harmonics drop by one or two orders of magnitude when compared with calculations where the Coulomb potential is not included. To investigate the reason for the drop, we calculated the time-averaged phase of each trajectory $\langle S_e \rangle = S_e / (t_{end} - t_0)$ and the phase difference of each trajectory with

and without the Coulomb potential $\Delta S_e = \langle S_e^C \rangle - \langle S_e^{NC} \rangle$. $\langle S_e^C \rangle$ is the time-averaged phase with the Coulomb potential and $\langle S_e^{NC} \rangle$ is the phase without the Coulomb potential. Here t_0 is the initial time and t_{end} is the end time of the laser pulse. We then ordered these trajectories according to phase difference from small to large, as 1st, 2nd, ..., m th. Figure 4(b) shows these arranged phase difference. Note that we have taken the test of the ΔS_e calculated in a half optical cycle, one optical cycle, and whole pulse duration. Due to the periodicity of laser electric field, similar results as in Fig. 4(b) can be obtained. In Fig. 4(c), we count the weights of the trajectories with different ΔS_e . As shown in Figs. 4(b) and 4(c), most trajectories have small phase differences. The distribution of weights is maximum when the phase difference is 0.18. Moreover, there are a few trajectories that have phase differences larger than 0.3. These latter trajectories account for about 3% of the total trajectories [from trajectory 0.97×10^6 to trajectory 1×10^6 trajectory, see also Fig. 4(c)]. The trajectories with the larger phase difference are heavily affected by the Coulomb potential. Based on Eqs. (12) and (13), we selected trajectories whose phase differences are greater than 0.3 to calculate the harmonic spectrum and compare it to the spectrum from trajectories where the phase difference is smaller than 0.3. Note that changing this value within the range of 0.3 ± 0.05 will not influence the conclusions. These two sets of harmonic spectra are shown in red lines (> 0.3) and blue lines (< 0.3) in Fig. 4(d). It shows that, in the plateau region, the harmonics generated from trajectories whose phase difference is smaller than 0.3 are dominant. In the near-threshold region, the main contribution to the harmonics is from trajectories whose phase differences are larger than 0.3.

We display the typical classical trajectory whose phase difference is larger than 0.3 in Fig. 5(a). For comparison, Fig. 5(b) shows the classical trajectory without the Coulomb potential under the same initial conditions. One can find that the electron under the Coulomb potential will orbit near the core. Therefore, we name these trajectories which have phase differences larger than 0.3 “orbiting trajectories,” which appear only when the Coulomb potential is present. On the other hand, there are electron trajectories that leave the ion core initially and then return to recollide with the core directly. They are nonorbiting trajectories and are not significantly affected by the Coulomb potential. Figure 5(c) displays the phase distributions of orbiting trajectories as a function of time. The color in Fig. 5(c) represents the phase of the m th trajectory at the given time. It can be found that the phase of the trajectory changes from 0 to 2π gradually within one-half cycle. Like the periodicity of the electric field, in the next half optical cycle, it will vary from 2π back to 0 periodically. Figure 5(e) is the weight of the trajectories with nearly 0 or 2π phase as a function of time and Fig. 5(g) is the time-frequency analysis of the harmonic spectrum generated from the orbiting trajectories. It is found that harmonics are generated over a broad time range (from 3.3 to 3.7 optical cycles) and only a few trajectories have a nearly 0 or 2π phase in a specific time and almost trajectory phase changes from 0 to 2π during this time interval. The large variation of phases of these trajectories leads to destructive interference from these orbiting trajectories and the reduction of the NTH yield. For the nonorbiting trajectories, Figs. 5(d) and 5(f) show that their

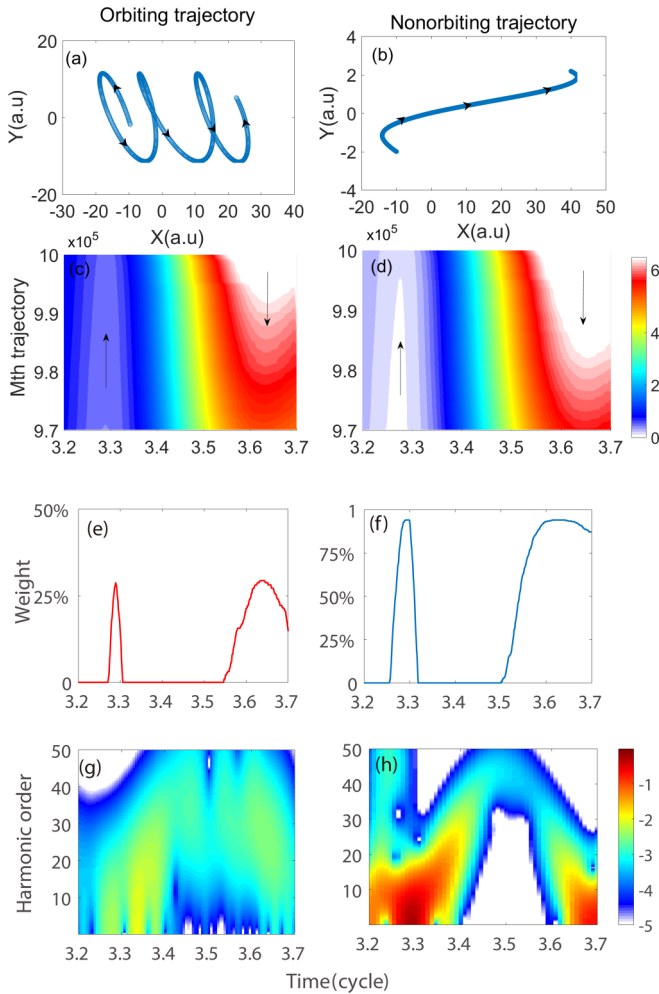


FIG. 5. The (a) orbiting trajectory and (b) nonorbiting trajectory (b) over one half optical cycle. The arrow represents the direction of electron motion. (c), (d) The phase of the orbiting and nonorbiting trajectories, respectively, over one-half optical cycles. The color represents the phase of the m th trajectory at the given time. (e), (f). The weight of the orbiting (red line) and nonorbiting trajectories (blue line) with nearly 0 or 2π phase. (g), (h) Time-frequency analysis of harmonics generated using orbiting and nonorbiting trajectories. Vertical scale is the harmonic order. Panel (g) shows that harmonics are emitted over a longer duration and the intensity is weaker. Panel (h) shows that harmonics are emitted over a short time duration and much stronger.

phases are almost the same for the interval of 3.25 to 3.35 optical cycles, and the phase varies only from 0 to 0.2 radians. These trajectories will interfere constructively. Indeed, the time-frequency analysis in Fig. 5(h) shows that the NTH yield generated from the nonorbiting trajectories is one order of magnitude higher than the yield generated from the orbiting trajectories. Comparing these two results, we find that, for trajectories affected by the Coulomb potential, the electron will orbit near the core to acquire larger phases, leading to destructive interference and depression of the NTH yields.

Next, we investigate how the abundance of orbiting trajectories and the depression of NTH are affected by the ellipticity of the driving laser. Figure 6(a) shows the orbiting trajectories

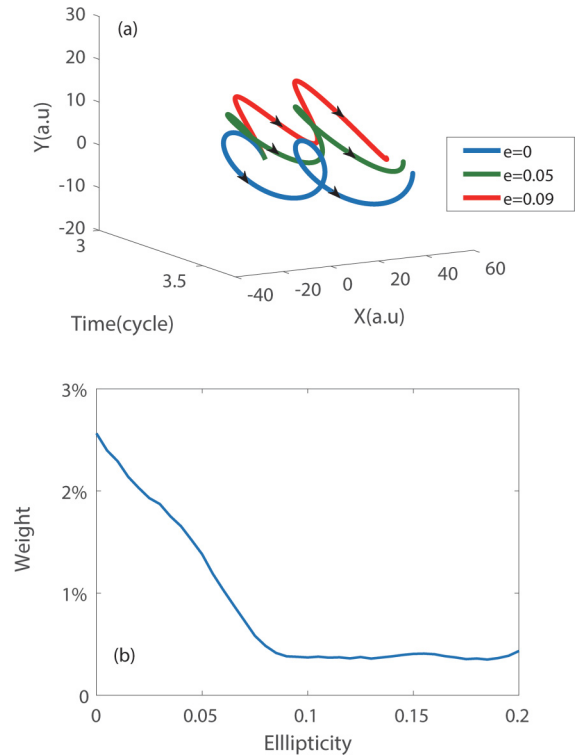


FIG. 6. (a) The orbiting trajectories for different laser ellipticities, for $\varepsilon = 0, 0.05, 0.09$, respectively. (b) The percentage of orbiting trajectories as a function of laser ellipticity ε .

for three different values of ε . When $\varepsilon = 0$, the electron orbits near the core. Under this condition, as discussed above, the Coulomb potential will introduce additional phase and lead to destructive interference between the trajectories. With the increase of ε , the electric field polarized along the \bar{y} direction is increased to break the orbiting. As the ε reaches 0.09, the electron would no longer be able to orbit. With even higher ellipticity, the electron would leave the core very quickly, reducing the contribution of orbiting trajectories to nil.

Figure 6(b) displays the weight of orbiting trajectories as a function of laser ellipticity. One can see that, when $\varepsilon = 0$, the weight of these trajectories is maximum. Due to destructive interference, the NTH yield is minimum. With increasing ellipticity, the number of orbiting trajectories drops, and the destructive interference is reduced, thus the NTH yield is higher than when laser ellipticity is zero. When ε is 0.09, the weight of orbiting trajectories reaches the minimum (0.5%). Note that, in Fig. 4(d), we have shown that the near-threshold harmonics mainly result from these orbiting trajectories, which account for 3% of the total trajectories when $\varepsilon = 0$. Therefore, $\varepsilon = 0.09$ causes a large drop in the orbiting trajectory. In this case, the yield of NTH will be enhanced by 1.2 to 1.5 times (see Fig. 3) when compared with the NTH yield at $\varepsilon = 0$. With the laser ellipticity continuing to increase, the weight of orbiting trajectories is no longer reduced, but the electron will move away quickly from the core, thus the harmonic yield will drop continuously.

Figure 7 shows the measured ellipticity dependence of the He, Ne, Ar, and Xe harmonic yields, for harmonics from 7 to 15 and the simulation from the QTMC model is given in

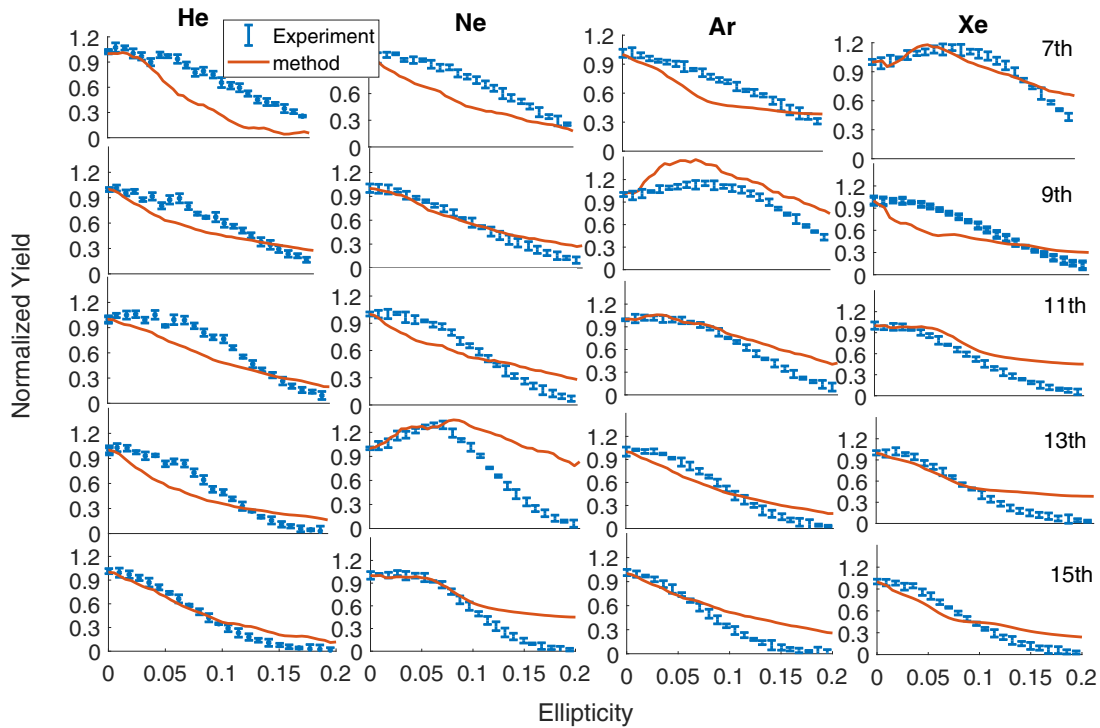


FIG. 7. The measured (markers) ellipticity dependence of He, Ne, Ar, and Xe for harmonic order from 7th to 15th. The laser intensity is about 2×10^{14} W/cm² and the max error (standard deviation) of our experiment data is about 7%. The results from QMTC are given as red lines.

red lines. In each graph, the harmonic yields are normalized to the yield at $\varepsilon = 0$. For helium, the harmonic yields from the experiment drop monotonically with ε except for the 11th harmonic where the yield reaches 1.05 at $\varepsilon = 0.05$. Our calculation was unable to reveal the anomaly. For neon, anomalous ellipticity dependence occurs for the 13th harmonic with a maximum yield of 1.29 when ellipticity is 0.08. The theory predicts more monotonic drop with ε and for higher ε the drop is more severe for higher harmonics than the theory predicts. For argon, clear anomalous ellipticity dependence occurs for the 9th harmonic, with a yield of 1.15, with an ellipticity of 0.1. The 11th harmonic also shows a weak anomaly with a yield of 1.05 at an ellipticity of 0.05. For krypton, the anomaly has been observed for the 7th and 9th harmonics (see Fig. 3). For xenon, the anomaly occurs at the 7th harmonic with a yield of 1.12 when the ellipticity is 0.09. Comparing our calculated results with the experiment, the harmonic order and the position of the maximal anomaly from experiments are mostly reproduced but discrepancies still occur in some results. Note that all the data shown in Fig. 7 are taken at the same laser intensity. This is quite a challenge since these targets have vast differences in ionization rates at the same intensity. In the QMTC calculations, each atom is modeled by a screened soft-core potential. The parameter α for each atom is chosen such that it gives the correct ionization potential. The values of α are 15.70, 4.10, 5.24, 5.70 for He, Ne, Ar, and Xe, respectively. The discrepancies between theory and experiment mainly result from three factors: (1) the uncertainty of the estimated laser parameters, (2) the possible propagation effect in experiment, and (3) the error of the calculated initial momentum distribution based on the ADK model. It has been

shown [48] that the center of the transverse momentum distribution has a shift when the atom is driven by an elliptically polarized laser field.

As has been discussed above, the existence of anomalous ellipticity dependence results from the orbiting trajectory electrons. Since each trajectory depends on the initial condition at ionization, in Fig. 8(a), we analyze the statistics of the initial momentum distributions of electrons that evolve as orbiting trajectories, for the case of Kr. The laser parameters are the same as those used in Fig. 3. Our simulation shows that the initial momentum for such orbiting trajectories has a Gaussian distribution around $(p_x, p_y) = (-0.1, -0.1)$, with the full width at half maxima (FWHM) of 0.1. The color coding in Fig. 8(a) shows the percent of trajectories that have initial momenta on the p_x - p_y plane. In Fig. 8(b), we show how the calculated ellipticity dependence of the

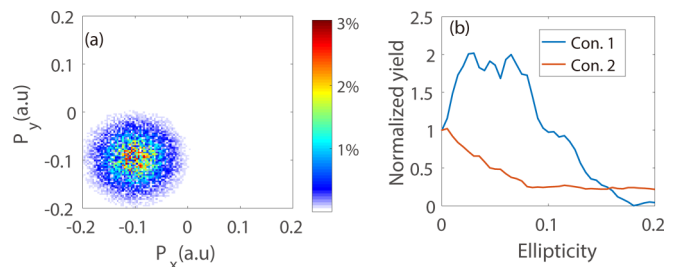


FIG. 8. (a) The initial momentum distribution of the electrons after ionization that emerge into orbiting trajectories. (b) The ellipticity dependence of model atom whose initial momentum distribution is around $(p_x, p_y) = (-0.1, -0.1)$ (Con. 1) and $(0.0, 0.0)$ (Con. 2).

harmonic yield varies with initial momentum distribution. For this purpose, we choose a Gaussian-type momentum distribution with FWHM width of 0.02, with the center at $(p_x, p_y) = (-0.1, -0.1)$ [Con. 1 in Fig. 8(b)], and another with the center at $(p_x, p_y) = (0.0, 0.0)$ [Con. 2 in Fig. 8(b)]. Clearly, in Fig. 8(b), it shows that the ellipticity dependence of harmonic yields for the former shows a strong anomaly, while for the latter the harmonic yield drops precipitously as ε increases. This result establishes that anomalous ellipticity dependence of near-threshold harmonics is due to electrons with orbiting trajectories, which in turn is determined by the special initial momentum distribution after electrons are released by tunneling.

Since the initial momentum distributions depend on the target as well as the laser intensity, we expect that the anomalous ellipticity dependence would depend on the atomic (and molecular) targets, as well as the laser intensity. According to the ADK model, the initial momentum distributions of the ionized electrons have a Gaussian distribution with the center at $(p_x = 0, p_y = 0)$. The FWHM of the initial momentum distribution is given by [35,36]

$$V_{FWHM} \propto \sqrt{\ln 2} \sqrt{\frac{E_0}{\sqrt{2}I_p}}, \quad (15)$$

where E_0 is the maximum electric field. Thus, the higher I_p is, the narrower the FWHM of the initial momentum distribution. For helium, it has the narrowest initial momentum distribution (0.15 with our laser parameters) among the noble gases. Thus, anomaly in ellipticity dependence is hardest to observe.

Finally, in Fig. 9(a) we look at the dependence of anomalous ellipticity on the intensity of the driving laser, using the 9th harmonic of Kr as an example. It is found that, at the low intensity of 1.5×10^{14} W/cm², the 9th harmonic yield of Kr decreases monotonically with increasing ε , which is in stark contrast with the anomalous dependence observed at the higher intensity of 2×10^{14} W/cm². The observed ellipticity dependence for these two intensities is accurately confirmed by our theoretical calculations. In Fig. 9(b), we show the calculated ellipticity dependence of the 9th harmonic of krypton at different laser intensities based on our model. It shows that, at low intensity ($< 1.7 \times 10^{14}$ W/cm²), the harmonic yield of Kr decreases monotonically with increasing ellipticity. With further increase of intensity, the anomalous ellipticity dependency of the 9th harmonic of krypton gradually becomes obvious. From Eq. (15), a lower intensity will make the initial momentum distribution of the ionized electron narrower, thus limiting the contribution from orbiting electrons to prevent the appearance of anomalous ellipticity dependence.

V. SUMMARY AND CONCLUSION

In summary, we have investigated the ellipticity dependence of harmonic yields of rare-gas atoms of He, Ne, Ar, Kr, and Xe for near-threshold harmonics (NTH). Experimentally, we found that, for each noble-gas atom, the yield of NTH would exhibit an anomaly, meaning that the harmonic yield does not drop monotonically as the laser's ellipticity ε is increased. The anomaly occurs for all noble-gas atoms studied, but He shows the weakest dependence. The NTH

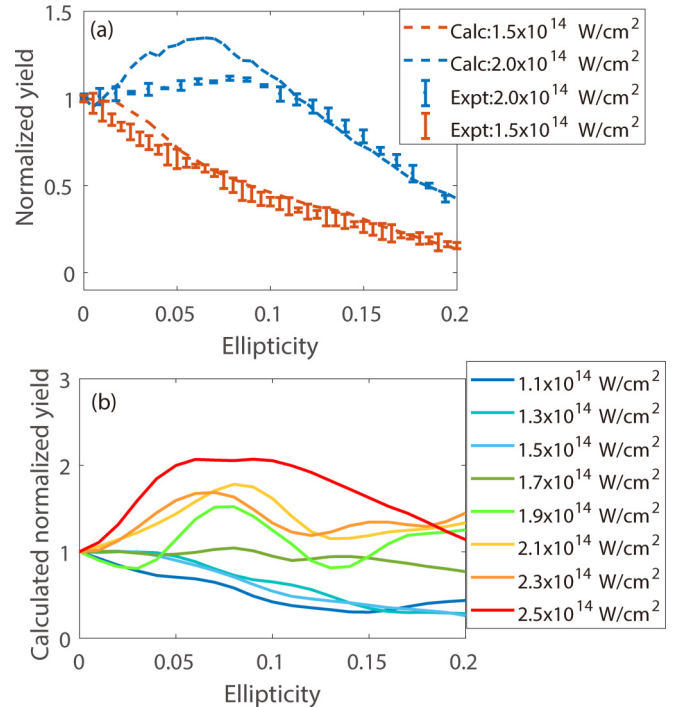


FIG. 9. (a) The measured and calculated ellipticity dependence at two different laser intensities for the 9th harmonic of krypton. (b) The calculated ellipticity dependence of the 9th harmonic of krypton at different laser intensities based on QTMC.

that exhibits anomaly depends on the species and laser intensity. To understand these experimental results we carried out QTMC calculations for the generation of NTH. It was found that the Coulomb potential between the ion core and the ionized electron is crucial for the appearance of anomalous ellipticity dependence. The QTMC simulation further offers an interpretation of the origin of the anomaly. With the presence of the Coulomb potential and the laser field, it was found that a certain small fraction of electrons would undergo orbiting in that the electron does not escape from the ion immediately. Instead, the electron can orbit around the ion core a number of times before escape. In the process, such delayed escape introduces a larger phase (or action) associated with each trajectory. The result of the destructive interference of these trajectories has been found to be the reason for the observed anomaly of the ellipticity dependence of the yield of NTH.

While it has long been recognized that the Coulomb potential is important for any strong-field processes near (below or above) the ionization threshold, precisely what role the Coulomb potential plays is more difficult to understand, especially within the time-dependent Schrödinger equation picture. Using the QTMC picture, by invoking classical trajectories and associating each trajectory with a phase, the role of the Coulomb potential becomes more apparent. As demonstrated in this article, the combining laser field and the Coulomb potential allows the appearance of orbiting in the classical sense, or the orbiting of the wave packet in the quantum sense. With the QTMC, the orbiting that appears in classical physics is easily understood. In NTH, on the other hand, it is the phase (or action), or more precisely, the interference from

different trajectories, that are responsible for the occurrence of the anomaly of harmonic yields versus ellipticity of the laser. These orbiting trajectories could be qualitatively related to Rydberg states [24]. More precisely, the wave packet describing these orbiting electrons are made of Rydberg states. Since Rydberg states exist only in the presence of a Coulomb potential, near-threshold phenomena occurring in strong fields cannot be explained without accounting for the Coulomb potential. A pure quantum formulation of a theory in this energy region would be required to treat Rydberg states correctly, but this cannot be easily done in view of the dense density of Rydberg states. The QTMC method employed here seems a good model for understanding near-threshold phenomena in strong-field physics.

ACKNOWLEDGMENTS

This work is supported by National Key R&D Program (2017YFE0116600, 2019YFA0307700); National Natural Science Foundation of China (Grants No. 91950202, No. 11627809, No. 11874165, No. 11774109, No. 11934006, and No. 12021004). The research of C.D.L. is supported by the Chemical Sciences, Geosciences, and Biosciences Division, Office of Basic Energy Sciences, Office of Science, U.S. Department of Energy, under Grant No. DE-FG02-86ER13491.

Bincheng Wang and Yinfu Zhang contributed equally to this work.

APPENDIX

In this Appendix, we show the detailed derivation from Eq. (6) to (8). The harmonics are generated from the recombination between a final state $|\psi_f\rangle$ and an initial state $|\psi_i\rangle$. The induced dipole between these two states is

$$d_{if} = \langle \psi_f | \vec{A}(\vec{r}, t) \cdot \vec{\nabla} | \psi_i \rangle, \quad (\text{A1})$$

where $\vec{A}(\vec{r}, t)$ is the electric vector potential and for a monochromatic light $\vec{A}(\vec{r}, t) = A_0(\omega) \cos(\vec{k} \cdot \vec{r} - \omega t) \hat{\epsilon}$. $\hat{\epsilon}$ is the polarization vector. Therefore, the induced dipole is [3]:

$$d_{if} = A_0(\omega) \langle \psi_f | e^{-i\vec{k} \cdot \vec{r}} \hat{\epsilon} \cdot \vec{\nabla} | \psi_i \rangle. \quad (\text{A2})$$

In the dipole approximation, it is written as

$$d_{if} = A_0(\omega) \hat{\epsilon} \langle \psi_f | \vec{\nabla} | \psi_i \rangle. \quad (\text{A3})$$

According to the Eqs. (A.2) and (A.3), at a given time t_1 , the final state $|\psi_f\rangle$ can be expressed as

$$|\psi_f\rangle = \sum_N e^{-i \int_0^{t_1} (L_0 + L_e) dt} |\psi_i\rangle. \quad (\text{A4})$$

Based on the formula

$$e^{\hat{A} + \hat{B}} = e^{\hat{A}} e^{\hat{B}} e^{\frac{1}{2}[\hat{A}, \hat{B}]}, \quad (\text{A5})$$

the term $e^{-i \int_0^{t_1} (L_0 + L_e) dt}$ can be split as

$$e^{-i \int_0^{t_1} (L_0 + L_e) dt} = e^{-i \int_0^{t_1} L_0 dt} e^{-i \int_0^{t_1} L_e dt} e^{-\frac{1}{2} i \int_0^{t_1} (-i\hbar\vec{k}) dt}, \quad (\text{A6})$$

where we have used $[L_0, L_e] = [T, -V_e] = -i\hbar\vec{k}$ using Eq. (5) in the main text. Therefore, the final state $|\psi_f\rangle$ is

$$|\psi_f\rangle = \sum_N e^{-i \int_0^{t_1} L_0 dt} e^{-i \int_0^{t_1} L_e dt} e^{-\frac{1}{2} i \int_0^{t_1} (-i\hbar\vec{k}) dt} |\psi_i\rangle. \quad (\text{A7})$$

Inserting Eq. (A.7) into Eq. (A.3), we obtain the induced dipole:

$$\begin{aligned} d_{if} &= A_0(\omega) \hat{\epsilon} \sum_N \langle \psi_i | e^{\frac{1}{2} i \int_0^{t_1} (-i\hbar\vec{k}) dt} e^{i \int_0^{t_1} L_e dt} \\ &\quad \times e^{i \int_0^{t_1} L_0 dt} \vec{\nabla} | \psi_i \rangle, \\ d_{if} &= A_0(\omega) \hat{\epsilon} \sum_N \int \psi_i^* e^{\frac{1}{2} i \int_0^{t_1} (-i\hbar\vec{k}) dt} e^{i \int_0^{t_1} L_e dt} \\ &\quad \times e^{i \int_0^{t_1} L_0 dt} \vec{\nabla} \psi_i dr. \end{aligned} \quad (\text{A8})$$

If a operator is Hermitian operator, we have the formula

$$\langle \psi | \hat{O} \varphi \rangle = \langle \hat{O}^+ \psi | \varphi \rangle. \quad (\text{A9})$$

Thus we have

$$\begin{aligned} d_{if} &= A_0(\omega) \hat{\epsilon} \sum_N \int e^{-i \int_0^{t_1} L_e dt} e^{-\frac{1}{2} i \int_0^{t_1} (-i\hbar\vec{k}) dt} \\ &\quad \times \psi_i^* e^{i \int_0^{t_1} L_0 dt} \vec{\nabla} \psi_i dr, \end{aligned} \quad (\text{A10})$$

where we have used

$$\begin{aligned} [e^{i \int_0^{t_1} L_e dt}]^+ &= e^{-i \int_0^{t_1} L_e dt}, \\ [e^{\frac{1}{2} i \int_0^{t_1} (-i\hbar\vec{k}) dt}]^+ &= e^{-\frac{1}{2} i \int_0^{t_1} (-i\hbar\vec{k}) dt}, \end{aligned} \quad (\text{A11})$$

and

$$(\hat{A}\hat{B})^+ = \hat{B}^+\hat{A}^+. \quad (\text{A12})$$

The factor $\psi_i^* e^{i \int_0^{t_1} L_0 dt}$ is the solution of the Schrödinger equation of an electron with momentum k in the potential V_c :

$$\left[-\frac{1}{2} \vec{\nabla}^2 + V_c \right] \psi_i(\mathbf{r}) = E \psi_i(\mathbf{r}), \quad E = \frac{k^2}{2}. \quad (\text{A13})$$

From Ref. [41], the solution of this Schrödinger equation is

$$e^{-i \int_0^{t_1} L_0 dt} \psi_i(\vec{r}) = \frac{1}{(2\pi)^{3/2}} \frac{f^{(\pm)}(\hat{k} \cdot \hat{r})}{\vec{r}} \exp(i\vec{k} \cdot \vec{r}). \quad (\text{A14})$$

This wave function is an outgoing (+) or incoming (−) spherical wave. The function $f^{(\pm)}(\hat{k} \cdot \hat{r})$ is called the scattering amplitude and can be obtained as

$$\begin{aligned} f^{(+)}(\hat{k} \cdot \hat{r}) &= \frac{1}{2ik} \sum_l (2l+1) [\exp(2i\delta_{El}) - 1] P_l(\cos\theta), \\ f^{(-)}(\hat{k} \cdot \hat{r}) &= \frac{1}{2ik} \sum_l (-1)^l (2l+1) \\ &\quad \times [1 - \exp(-2i\delta_{El})] P_l(\cos\theta), \end{aligned} \quad (\text{A15})$$

where the $P_l \cos(\theta)$ is the Legendre function, l is the angular momentum which ranges from 0 to ∞ , and E is the energy of the electron state including the bound state (Rydberg states)

and the continuous state. We can insert Eq. (A.14) into Eq. (A.10):

$$d_{if} = A_0(\omega)\hat{\epsilon} \sum_N \int e^{-i \int_0^{t_1} L_e dt} e^{-\frac{1}{2}i \int_0^{t_1} (-i\hbar\vec{k}) dt} \times \frac{1}{(2\pi)^{3/2}} \frac{f^{(\pm)}(\hat{k} \cdot \hat{r})}{\vec{r}} \exp(-i\vec{k} \cdot \vec{r}) \vec{\nabla} \psi_i dr. \quad (\text{A16})$$

The factor $\frac{1}{(2\pi)^{3/2}} \frac{f^{(\pm)}(\hat{k} \cdot \hat{r})}{\vec{r}} \exp(-i\vec{k} \cdot \vec{r}) \vec{\nabla} \psi_i$ is similar to the form of the transition dipole moment and can be defined as

$$\frac{1}{(2\pi)^{3/2}} \frac{f^{(\pm)}(\hat{k} \cdot \hat{r})}{\vec{r}} \exp(-i\vec{k} \cdot \vec{r}) \vec{\nabla} \psi_i = \sigma_N(E, \theta), \quad (\text{A17})$$

where $E = k^2/2$ is the energy of the electron and $\theta = \text{atan}(k_y/k_x)$ is the angle of the electron momentum.

The remaining term $e^{-i \int_0^{t_1} L_e dt} e^{-\frac{1}{2}i \int_0^{t_1} (-i\hbar\vec{k}) dt}$ is the propagator induced by the laser field and will be denoted as

$$e^{-i \int_0^{t_1} L_e dt} e^{-\frac{1}{2}i \int_0^{t_1} (-i\hbar\vec{k}) dt} = U_N(E, \theta). \quad (\text{A18})$$

Therefore, we obtain the final form of the induced dipole for the harmonic generation at a given time t_1 :

$$d_{if}(t_1) = A_0(\omega)\hat{\epsilon} \sum_N \int U_N(E, \theta) \sigma_N(E, \theta) dr. \quad (\text{A19})$$

In the laser field, the energy of the electron E and the angle of the electron momentum θ varies with time. Therefore, at any time for each trajectory N we can acquire the energy of the electron $E(t)$ and the angle of the electron momentum $\theta(t)$. Inserting these two terms into the Eq. (A.15), the time-dependent induced dipole is

$$d(t) = A_0(\omega)\hat{\epsilon} \sum_N \int U_N(E(t), \theta(t)) \sigma_N(E(t), \theta(t)) dr. \quad (\text{A20})$$

-
- [1] F. Krausz and M. Ivanov, *Rev. Mod. Phys.* **81**, 163 (2009).
- [2] M. Hentschel, R. Kienberger, Ch. Spielmann, G. A. Reider, N. Milosevic, T. Brabec, P. Corkum, U. Heinzmann, M. Drescher, and F. Krausz, *Nature (London)* **414**, 509 (2001).
- [3] C. D. Lin, A. T. Le, C. Jin, and H. Wei, *Attosecond and Strong-Field Physics: Principles and Applications* (Cambridge University Press, Cambridge, England, 2018).
- [4] G. Sansone, E. Benedetti, F. Calegari, C. Vozzi, L. Avaldi, R. Flammini, L. Poletto, P. Villoresi, C. Altucci, R. Velotta *et al.*, *Science* **314**, 443 (2006).
- [5] D. C. Yost, T. R. Schibli, J. Ye, J. L. Tate, J. Hostetter, M. B. Gaarde, and K. J. Schafer, *Nat. Phys.* **5**, 815 (2009).
- [6] T. Popmintchev *et al.*, *Science* **336**, 1287 (2012).
- [7] C. Zhai, R. Shao, P. Lan, B. Wang, Y. Zhang, H. Yuan, S. M. Njoroge, L. He, and P. Lu, *Phys. Rev. A* **101**, 053407 (2020).
- [8] J. Itatani, J. Levesque, D. Zeidler, H. Niikura, H. Pepin, J. C. Kieffer, P. B. Corkum, and D. M. Villeneuve, *Nature (London)* **432**, 867 (2004).
- [9] B. N. Wang, L. X. He, Y. Q. He, Y. F. Zhang, R. Z. Shao, P. F. Lan, and P. X. Lu, *Opt. Express* **27**, 30172 (2019).
- [10] S. Haessler, J. Caillat, W. Boutu, C. Giovanetti-Teixeira, T. Ruchon, T. Auguste, Z. Diveki, P. Breger, A. Maquet, B. Carre *et al.*, *Nat. Phys.* **6**, 200 (2010).
- [11] C. Vozzi, M. Negro, F. Calegari, G. Sansone, M. Nisoli, S. D. Silvestri, and S. Stagira, *Nat. Phys.* **7**, 822 (2011).
- [12] K. Liu, M. Li, W. H. Xie, K. Y. Guo, S. Q. Luo, J. Q. Yan, Y. M. Zhou, and P. X. Lu, *Opt. Express* **28**, 12439 (2020).
- [13] L. Li, P. F. Lan, L. X. He, W. Cao, Q. B. Zhang and P. X. Lu, *Phys. Rev. Lett.* **124**, 157403 (2020).
- [14] P. B. Corkum, *Phys. Rev. Lett.* **71**, 1994 (1993).
- [15] K. J. Schafer, B. Yang, L. F. DiMauro, and K. C. Kulander, *Phys. Rev. Lett.* **70**, 1599 (1993).
- [16] M. Lewenstein, Ph. Balcou, M. Y. Ivanov, A. L'Huillier, and P. B. Corkum, *Phys. Rev. A* **49**, 2117 (1994).
- [17] M. Chini, X. Wang, Y. Cheng, H. Wang, Y. Wu *et al.* *Nat. Photonics* **8**, 437 (2014).
- [18] C. Gohle, T. Udem, M. Herrmann, J. Rauschenberger, R. Holzwarth, H. A. Schuessler, F. Krausz, and T. W. Hänsch, *Nature (London)* **436**, 234 (2005).
- [19] A. Cingöz, D. C. Yost, T. K. Allison, A. Ruehl, M. E. Fermann, I. Hartl, and J. Ye, *Nature (London)* **482**, 68 (2012).
- [20] H. Yun and J. H. Mun, S. I. Hwang *et al.*, *Nat. Photonics* **12**, 620 (2018).
- [21] W. H. Xiong, J. W. Geng, J. Y. Tang, L. Y. Peng, and Q. Gong, *Phys. Rev. Lett.* **112**, 233001 (2014).
- [22] P. Li, Y. Sheu, C. Laughlin, and S. Chu, *Nat. Commun.* **6**, 7178 (2015).
- [23] E. P. Power, A. M. March, F. Catoire, E. Sistrunk, K. Krushelnick, P. Agostini, and L. F. DiMauro, *Nat. Photonics* **4**, 352 (2010).
- [24] W. H. Xiong, X. R. Xiao, L. Y. Peng, and Q. Gong, *Phys. Rev. A* **94**, 013417 (2016).
- [25] T. Nubbemeyer, K. Gorling, A. Saenz, U. Eichmann, and W. Sandner, *Phys. Rev. Lett.* **101**, 233001 (2008).
- [26] Y. Zhao, Y. Zhou, J. Liang, Z. Zeng, Q. Ke, Y. Liu, M. Li, and P. Lu, *Opt. Express* **27**, 21689 (2019).
- [27] L. He, P. Lan, C. Zhai, Y. Li, Z. Wang, Q. Zhang, and P. Lu, *Phys. Rev. A* **91**, 023428 (2015).
- [28] M. Kakehata, H. Takada, H. Yumoto, and K. Miyazaki, *Phys. Rev. A* **55**, R861 (1997).
- [29] N. H. Burnett, C. Kan, and P. B. Corkum, *Phys. Rev. A* **51**, R3418 (1995).
- [30] K. Miyazaki and H. Takada, *Phys. Rev. A* **52**, 3007 (1995).
- [31] H. Soifer, P. Botheron, D. Shafir, A. Diner, O. Raz, B. D. Bruner, Y. Mairesse, B. Pons, and N. Dudovich, *Phys. Rev. Lett.* **105**, 143904 (2010).
- [32] A. Ferré *et al.*, *Nat. Commun.* **6**, 5952 (2015).
- [33] M. Yu. Ivanov, T. Brabec, and N. Burnett, *Phys. Rev. A* **54**, 742 (1996).
- [34] K. Avnani *et al.*, *J. Phys. B: At., Mol. Opt. Phys.* **49**, 114002 (2016).

- [35] J. A. Hostetter, J. L. Tate, K. J. Schafer, and M. B. Gaarde, *Phys. Rev. A* **82**, 023401 (2010).
- [36] M. Li, J. W. Geng, H. Liu, Y. Deng, C. Wu, L. Y. Peng, Q. Gong, and Y. Liu, *Phys. Rev. Lett.* **112**, 113002 (2014).
- [37] Y. Q. He, L. X. He, P. Wang, B. C. Wang, S. Q. Sun, R. X. Liu, B. N. Wang, P. F. Lan, and P. X. Lu, *Opt. Express* **28**, 21182 (2020).
- [38] B. C. Wang, Y. Q. He, X. Zhao, L. X. He, and P. F. Lan, P. X. Lu and C. D. Lin, *Phys. Rev. A* **101**, 063417 (2020).
- [39] http://henke.lbl.gov/optical_constants/.
- [40] R. P. Feynman, *Rev. Mod. Phys.* **20**, 367 (1948).
- [41] F. Salvat, J. M. Fernández-Varea, *Comput. Phys. Commun.* **90**, 151 (1995).
- [42] X. M. Tong, Z. X. Zhao, and C. D. Lin, *Phys. Rev. A* **66**, 033402 (2002).
- [43] V. P. Krainov, *J. Opt. Soc. Am. B* **14**, 425 (1997).
- [44] M. V. Ammosov, N. B. Delone, and V. P. Krainov, *Zh. Eksp. Teor. Fiz.* **91**, 2008 (1986) [*Sov. Phys.-JETP* **64**, 1191 (1986)].
- [45] A. M. Perelomov, V. S. Popov, and M. V. Terent'ev, *Zh. Eksp. Teor. Fiz.* **50**, 1393 (1966) [*Sov. Phys.-JETP* **23**, 924 (1966)].
- [46] A.-T. Le, R. R. Lucchese, S. Tonzani, T. Morishita, and C. D. Lin, *Phys. Rev. A* **80**, 013401 (2009).
- [47] W. Xiong *et al.*, *J. Phys. B: At., Mol. Opt. Phys.* **50**, 032001 (2017).
- [48] M. Han, M. Li, M. M. Liu, and Y. Liu, *Phys. Rev. A* **95**, 023406 (2017).